IEEE Access
Multidisciplinary | Rapid Review | Open Access Journal

Received August 30, 2018, accepted September 24, 2018, date of publication October 2, 2018, date of current version October 25, 2018.

Digital Object Identifier 10.1109/ACCESS.2018.2873500

Improving Molecular Sensitivity in X-Ray Fluorescence Molecular Imaging (XFMI) of Iodine Distribution in Mouse-Sized Phantoms via Excitation Spectrum Optimization

XU DONG[1], CHENG CHEN[2], AND GUOHUA CAO[1]
[1]Department of Biomedical Engineering and Mechanics, Virginia Polytechnic Institute and State University, Blacksburg, VA 24061, USA
[2]Department of Mining and Minerals Engineering, Virginia Polytechnic Institute and State University, Blacksburg, VA 24061, USA

Corresponding author: Guohua Cao (ghcao@vt.edu)

This work was supported in part by the Dr. Guohua Cao's CAREER Award from the U.S. National Science Foundation under Grant CBET 1351936, in part by the Alpha Foundation under Grant AFC518-40, and in part by the VT Open Access Subvention Fund.

ABSTRACT X-ray fluorescence molecular imaging (XFMI) has shown great promise as a low-cost molecular imaging modality for clinical and pre-clinical applications with high sensitivity. Recently, progress has been made in enabling the XFMI technique with laboratory X-ray sources for various biomedical applications. However, the sensitivity of XFMI still needs to be improved for *in vivo* biomedical applications at a reasonably low radiation dose. In laboratory X-ray source-based XFMI, the main factor that limits the molecular sensitivity of XFMI is the scatter X-rays that coincide with the fluorescence X-rays from the targeted material. In this paper, we experimentally investigated the effects of excitation beam spectrum on the molecular sensitivity of XFMI, by quantitatively deriving minimum detectable concentration (MDC) under a fixed surface entrance dose of 200 mR at three different excitation beam spectra. XFMI experiments were carried out on two customized mouse-sized phantoms. The result shows that the MDC can be readily increased by a factor of 5.26 via excitation spectrum optimization. Furthermore, a numerical model was developed and validated by the experimental data. The numerical model can be used to optimize XFMI system configurations to further improve the molecular sensitivity. Findings from this investigation could find applications for *in vivo* pre-clinical small-animal XFMI in the future.

INDEX TERMS Molecular imaging, X-ray fluorescence, molecular sensitivity.

I. INTRODUCTION

X-ray Fluorescence Molecular Imaging (XFMI) as an imaging technique for elemental mapping or bio-distribution studies of a target molecule in a biological body has a great potential for applications in personal or precision medicine for many diseases such as cancers. XFMI utilizes the secondary x-ray fluorescence signal to map out the distribution information of specific elements. In XFMI, external x-rays are used to produce the secondary fluorescence x-rays via the interactions between the excitation x-ray photons and the target elements in the imaged object. Because the energies of the generated fluorescence x-ray photons are characteristic to the target elements, the spatial distribution of individual element species can be derived from their corresponding x-ray fluorescence signals.

The XFMI technique was first investigated for biological applications by Ahlgren *et al.* [1] by measuring lead in organs near the skin's surface using a synchrotron source. Since then, the synchrotron-based XFMI technique has been widely investigated over the past decades for different biomedical applications [2]–[5]. The combination of XFMI technique with other imaging modalities has been investigated recently. For example, the combination of XFMI and micro-Computed Tomography (micro-CT) has been demonstrated in 2000 [6]. More recently, the XFMI technique has been adopted to quantitatively detect novel imaging contrast agents, such as nanoparticles based on iodine and gold, at low concentrations for specific biological purposes. Examples include the XFMI imaging of gold nanoparticle-based contrast agent to detect tumor locations [7], [8], and the XFMI imaging of iodine

2169-3536 © 2018 IEEE. Translations and content mining are permitted for academic research only.
Personal use is also permitted, but republication/redistribution requires IEEE permission.
See http://www.ieee.org/publications_standards/publications/rights/index.html for more information.

perfusion in a mouse brain [9]. All these experiments employed monochromatic x-rays generated by the synchrotron sources. However, due to the limited availability and the high cost of synchrotron radiations, synchrotron-based XFMI technique has not been widely applied to clinical or pre-clinical research.

The feasibility of XFMI technique using laboratory x-ray sources was demonstrated rather recently in 2010 [10]. Enabling XFMI with conventional x-ray sources gives the technique a big boost to its potential in routine clinical or pre-clinical applications. In the past a few years, several studies have been conducted to examine the feasibility of enabling XFMI using conventional x-ray sources [11]–[22]. For instances, Jones *et al.* [13] successfully built a bench-top cone beam x-ray fluorescence CT system in 2012, Kuang *et al.* [14] utilized the XFMI technique to trace the distributions of three different elements simultaneously in 2013, Ren *et al.* [16] implemented a pixel-mapping based XFMI for element analysis in 2014, Yoon *et al.* [18] developed a three dimension fluorescence CT system with CdTe detector array in 2016, and Li *et al.* [22] designed a full-field fan-beam x-ray fluorescence CT system in 2017. Most of the XFMI techniques utilized the K-shell fluorescence signals to obtain the element distribution, but XFMI using the L-shell fluorescence signals has also been investigated [23]–[25].

To adopt XFMI for biological applications, a main research focus is to increase molecular sensitivity at a biologically acceptable radiation dose. The sensitivity of the XFMI technique depends on a number of factors, including the targeted contrast agent, excitation x-ray spectrum, and acquisition geometry. XFMI imaging at different acquisition configurations has been investigated in several recent studies [11]–[19]. For imaging contrast agent, iodine [26], [27] and gold nanoparticles [28], [29] has been more extensively investigated because of their suitable x-ray fluorescence energies, high x-ray fluorescence yield, and good biochemical properties. A comprehensive comparison of different materials as XFMI contrast agents for biological applications can be found in [30].

One of the main factors that determine the molecular sensitivity in laboratory x-ray source based XFMI is the scatter x-ray background from the interactions between a polychromatic excitation x-ray beam and the imaged object. Many methods have been proposed to overcome the interfering scatter background x-ray photons. For example, the detector is typically placed perpendicular to the direction of the excitation x-ray beam to minimize the amount of scatter x-ray photons reaching the detector [31], and detector collimators are usually used to further reject the number of scatter photons reaching the detector [32]. Various data processing techniques based on curve fitting and statistical modeling have also been applied to subtract the scatter background x-ray photons [12], [25].

Another effective way to improve the molecular sensitivity of XFMI with laboratory x-ray sources is via optimizing the spectrum of the excitation x-ray beam [26], [33]. An intuitive explanation is that the scatter x-ray photons at the characteristic x-ray fluorescence energies of the targeted element would obscure the detected x-ray fluorescence peaks, resulting in lower XFMI sensitivity. Therefore, optimizing the excitation beam spectrum with a goal of suppressing the number of scatter photons at the characteristic x-ray fluorescence energies of the targeted element can be a viable strategy for improving molecular sensitivity for XFMI. For example, in a previous work we demonstrated that the molecular sensitivity in the XFMI of iodine-based contrast agent using a bremsstrahlung x-ray source can be improved via excitation spectrum optimization with simple x-ray filtrations [26]. However, a systematic and quantitative investigation on how the molecular sensitivity of XFMI depends on different spectra of the excitation beam has not been carried out, especially in the configuration of small animal XFMI.

XFMI of small animals, particularly mice and rats, will be valuable for many basic and preclinical studies for understanding the pathophysiology of disease [34], [35] and developing new drug candidates for cancer and cardiovascular disorders [36], [37]. This is especially true with the development of gene knockout and transgenic technologies. In this paper, we report our systematic and quantitative experimental investigations on improving the molecular sensitivity in XFMI of iodine distribution in mouse-sized phantoms via excitation spectrum optimization, with the goal of applying this technique for *in vivo* small-animal XFMI. Furthermore, we developed an XFMI simulation model and validated the model by the experimental data.

The paper is organized as follows. After the introduction, in section II we describe our experiments and methods, which contain the experimental setup, the data processing methods, and the XFMI system simulation. The results are shown in section III, followed by the discussions and conclusions in section IV.

II. EXPERIMENTS AND METHODS

A. EXPERIMENTAL SETUP

To investigate the effects of the excitation beam spectra on the molecular sensitivity of XFMI systems, we developed a bench-top XFMI setup using a laboratory bremsstrahlung x-ray source. A picture of the XFMI setup is shown in Fig. 1(A). It consists of a conventional x-ray source, a source beam filter, a source collimator, a mouse-sized phantom, and an energy-sensitive x-ray spectrometer with collimator. The XFMI geometry parameters and the experimental parameters are listed in Table 1.

1) X-RAY SOURCE AND FILTERS

A commercially available x-ray source (Thermo Kevex x-ray) was operated at 40 kV. It has a tungsten anode. A filter was placed near the x-ray source's exit window to shape the excitation x-ray beam spectrum. Different filter choices (materials and thickness) can lead to different excitation spectra. Three different filter choices were used in this study.

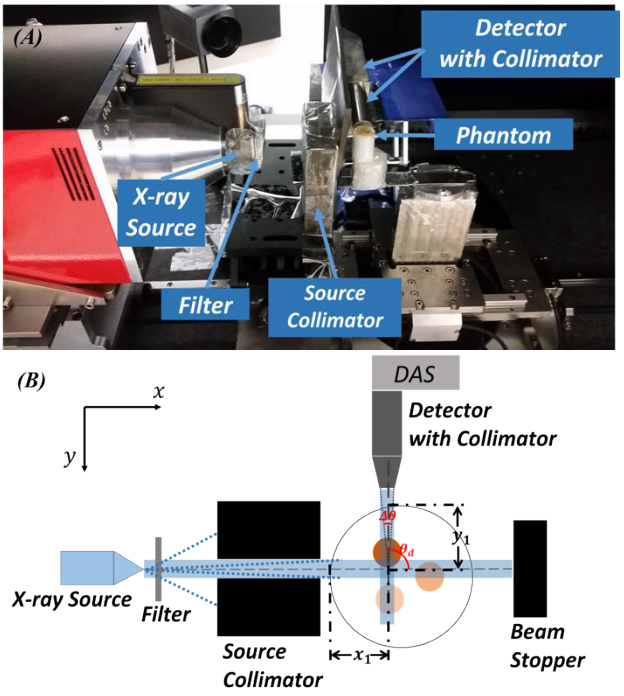

FIGURE 1. (A) A picture of the experimental setup. (B) A schematic of the XFMI configuration.

TABLE 1. Parameters of the XFMI Experiments.

Source to Object Distance	45 mm
Object to Detector Distance	30 mm
Collimators Aperture Size	3 mm
Phantom Diameter	20 mm
Phantom Vial Size	3 mm
Translational Step Size	3 mm
Source Voltage	40 kV
Radiation Dose Level	200 mR for calibration phantom 500 mR for contrast phantom

They are 1.02 mm Copper, 5.20 mm Aluminum, and 2.08 mm Aluminum. The spectra of the excitation x-ray beam after different filters were measured experimentally by placing the detector along the excitation beam path. And the experimentally measured excitation spectra were further validated with the simulations by the SpekCalc program [38].

As shown in Fig. 1, a source collimator was placed between the source filter and the object to shape the excitation x-ray beam into a pencil x-ray beam. The source collimator is made of alloy steel with a thickness of 3 cm and the aperture size of the collimator is 3 mm. This source collimator makes the cross section size of pencil beam passing through the object to be around 3 mm when the object is placed right next to the collimator.

2) X-RAY DETECTOR

The signals were detected by a CdTe detector (x-123CdTe, Amptek Inc). The detected signals were connected with a computer to collect and analyze the data. for this study, the detector was calibrated to collect x-ray photons from 0 kev to 43.73 kev with 2048 channels, resulting in the energy bin width of 21.35 ev per channel in the measured spectrum.

The detected x-rays consisted of the desired fluorescence x-ray photons from iodine and the undesired background x-ray photons which are mainly caused by the Compton scattering of the excitation x-ray photons. To minimize the number of Compton scatter x-ray photons reaching the x-ray detector, the detector was mounted at 90-degree to the excitation x-ray beam and installed with a detector collimator.

The detector collimator was placed in front of the x-ray detector to minimize the scatter x-ray photons that reach the detector. The wall thickness of the detector collimator is 2.5 cm, and its aperture size is 3 mm as well, which restricts the detector line of sight to be around 3 mm at its cross section (see Fig. 1). Under such geometry, only the x-ray photons originated from the pixel formed by the intersection of the excitation pencil x-ray beam and the detector line of sight can reach the x-ray detector. The pixel size from this collimation configuration is therefore 3 mm × 3 mm × 3 mm.

3) IMAGING PHANTOMS

Two mouse-sized phantoms were built for this study. Their illustrations are shown in Fig. 2. Both phantoms are made of 20-mm-diameter cylinders with the material of the phantoms as polymethyl methacrylate (PMMA). One is a calibration phantom (Fig. 2(A)), and the other is a contrast phantom (Fig. 2(B)).

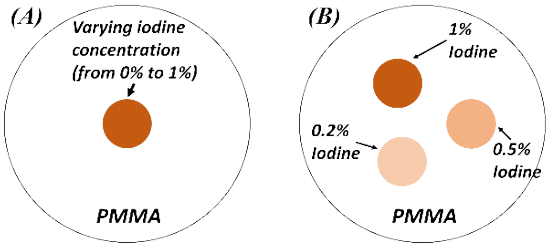

FIGURE 2. Schematics of the customized phantoms. (A) Calibration phantom with a single vial at the center. Different iodine solution with concentration of 1%, 0.5%, 0.25%, 0.167%, 0.125%, 0.1% and 0% (pure water) was inserted into the vial during each experiment. (B) The Contrast phantom with three vials filled with iodine solutions of different concentrations.

The calibration phantom contains a single 3-mm-diameter vial at its isocenter, which is filled with iodine solution of varying concentrations to find out the Minimum Detectable Concentration (MDC). In the calibration phantom study, the XFMI system is fixed and only the center voxel of the phantom, which corresponds to the center vial containing the iodine solution, was imaged. All the three filter options (1.02 mm Copper, 5.20 mm Aluminum, and 2.08 mm Aluminum) were used to generate three different excitation beam spectra. The phantom was aligned with the excitation beam path and the detector line of sight in such a way that only the signal generated from the vail containing iodine solutions

was able to reach the detector. For each excitation x-ray beam spectrum, a series of iodine solutions with concentrations at 1%, 0.5%, 0.25%, 0.167%, 0.125%, 0.1% and 0% (pure water) by weight (wt.), respectively, were inserted into the vial, and the resulted iodine fluorescence x-ray signals were measured at a fixed surface entrance dose of 200 mR. The series of measurements are used to derive the MDC for each excitation x-ray beam spectrum.

The contrast phantom contains three vials, which are filled with three iodine solutions at different concentrations to investigate the imaging contrast and the system linearity. All vials have a diameter of 3 mm. Iodine solutions with the concentrations of 1%, 0.5%, and 0.2% were inserted into the three vials, respectively. In the contrast phantom study, translational stepping movements of the detector and the phantom in the x and the y directions respectively were made to collect signals, which will finally result in an XFMI signal image in the dimension of 7 pixels by 7 pixels covering the whole contrast phantom. The accurate stepping movements were achieved by the linear stage. The generated XFMI signal image after data processing can be used to reflect the iodine distribution in the contrast phantom. The surface entrance dose level was set to be 500 mR. And the contrast phantom was imaged only by the two excitation spectra generated by the two Aluminum filter options (5.20 mm Aluminum and 2.08 mm Aluminum), mainly because of the long exposure time required to obtain the desired dose level when using the Copper filter.

4) EXPOSURE TIME AND RADIATION DOSE

In this study, the surface entrance dose was fixed at 200 mR for the experiments with the calibration phantom, and 500 mR for the experiments with the contrast phantom. To achieve the desired radiation dose, the exposure time (T) for different excitation spectrum was accordingly determined based on the characteristic dose factor (Γ) as the following:

$$T = \frac{D * d^2}{\Gamma * I}, \tag{1}$$

where D is the dose level, d is the distance between the source and the imaged object, I is the x-ray source current, and Γ is the characteristic dose factor for a given excitation spectrum, which is calculated using the SpekCalc program [38]. The exposure time for each experiment is listed in Table 2.

B. DATA PROCESSING

1) EXTRACTION OF FLUORESCENCE SIGNAL

Fig. 3 shows an example of the *measured x-ray fluorescence signals*collected by the Amptek detector from the XFMI setup described in section II.A. The iodine x-ray fluorescence signal contains two iodine fluorescence peaks, namely the k_α peak and the k_β peak. The centers of the two peaks are located at 28.6 keV and 32.3 keV, respectively. We set the window width for both fluorescence peaks at 2 keV in our data processing procedure. Therefore, the energy range from 27.6 keV to 29. 6 keV was considered as the k_α *fluorescence peak energy range*, and the energy range from 31.3 keV to 33.3 keV was considered as the k_β fluorescence peak energy range. All the other data outside the two fluorescence peak

TABLE 2. The exposure time for each experiment.

Different Excitation Spectra Group:	Characteristic Dose Factor ($\mu Gy/mA * s$ @ 1 meter)	X-ray Source Current Setup (mA)	Exposure Time for the Calibration Phantom [a] (sec.)	Exposure Time for the Contrast Phantom [b] (sec.)
1.02mm Cu filter:	0.009517	0.200	2127	N/A
5.20mm Al filter:	5.165561	0.010	78	196
2.08mm Al filter:	23.47016	0.005	34	86

To achieve a moderate and feasible exposure time for all the experiment, we used different x-ray source currents for different excitation spectra.

[a]For the calibration phantom (Fig. 2(A)), the dose level is set to be 200 mR.

[b]For the contrast phantom (Fig. 2(B)), the dose level is set to be 500 mR. And the copper filter is not used for the experiment.

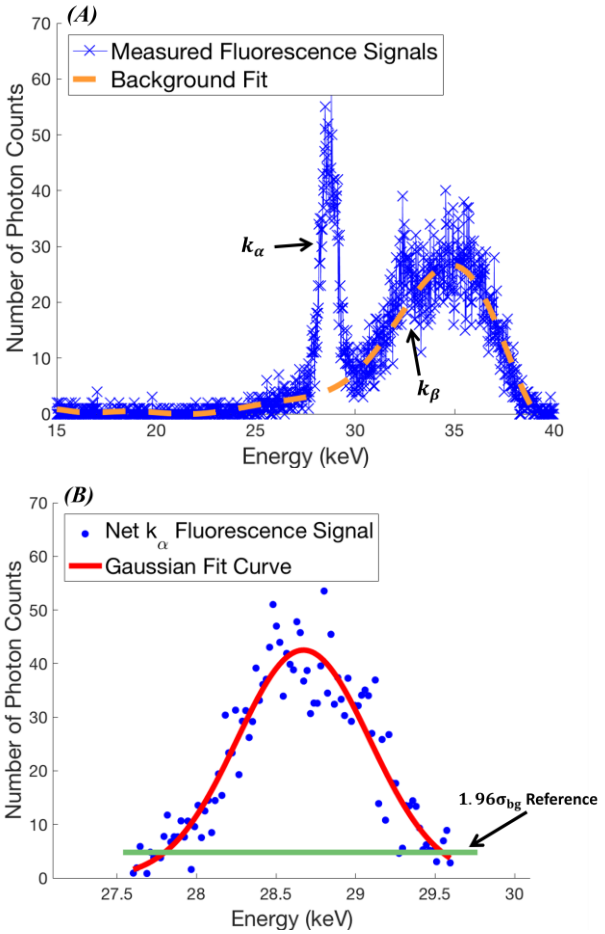

FIGURE 3. Illustration of the procedure for extracting net fluorescence signals. (A) Scatter background interpolation. The blue curve is the measured iodine fluorescence signal and the dashed orange line is the ten-order polynomial background fit from the off-peak range data. (B) Isolation of the net fluorescence signal. The blue dots represent the extracted net iodine k_α fluorescence signal, and the red curve is its Gaussian fit. The green line represents the reference level at $1.96\sigma_{bg}$.

energy ranges were considered the *off-peak energy range* data.

The first step in extracting the *net fluorescence signal* from a measured x-ray fluorescence signal is to find out the *scatter background signals* in the fluorescence peak energy ranges. For the off-peak energy range data, a ten-order polynomial least squares fit was applied to obtain the *off-peak background fit*. Then, the scatter background signals within the fluorescence peak energy ranges were obtained by the ten-order polynomial interpolations of the off-peak background fit. The interpolated scatter background signals (denoted as bg) were subtracted from the measured x-ray fluorescence signals at the fluorescence peak energy range to obtain the *net fluorescence signal*. In this study, we only used iodine fluorescence signal at the k_α peak, because the intensity of the k_β peak is barely visible in our low dose experiments.

After obtaining the net iodine fluorescence signal, it was fit with a Gaussian curve. The height (denoted as h) of the fitted Gaussian curve was taken as the *strength* of the net fluorescence signal, and hereafter it is referred as the *fluorescence peak height*. An illustration of the procedure for extracting fluorescence signal is illustrated in Fig. 3.

2) MINIMUM DETECTABLE CONCENTRATION

In this study, the Minimum Detectable Concentration (MDC) is used to characterize the molecular sensitivity of a XFMI system, which is a measure of the capability of the system to distinguish a net fluorescence signal (the fluorescence peak height (h)) from the random fluctuations of the background signal (bg). The random fluctuations of the background signal can be characterized by the background noise (σ_{bg}), which was treated as the mean of all the deviations between the experimentally measured data points and the fitted background values at the off-peak energy range. To be treated as distinguishable from the background fluctuations with 95% confidence level, the fluorescence peak height (h) must be larger than $1.96\sigma_{bg}$. In the calibration phantom study, a least squares linear fit was applied to the fluorescence peak heights (h) obtained at various iodine concentrations. Then the MDCs from different excitation spectra are determined by the intersecting points between the linear fit lines and the $1.96\sigma_{bg}$ reference lines, as shown in Fig. 3(B).

3) ATTENUATION CORRECTION

In the contrast phantom study, to generate a whole XFMI signal image, attenuation corrections must be performed to the net fluorescence signal obtained via the procedure described in the above section. As shown in Fig. 1(B), before the primary excitation beam reaches a pixel in the object, it experiences the attenuation by the path length x_1. Similarly, the generated secondary x-ray beam would also be attenuated by the path length y_1 before it could reach the detector. To ensure that the XFMI signal is proportional to the iodine concentration at each pixel location, the variation of primary beam attenuation and the secondary beam attenuation at different pixel location has to be corrected.

Henceforth, the attenuation correction factor (C) is calculated as:

$$C = \exp\left(\int_0^{x_1} \mu_p(x)dx + \int_0^{y_1} \mu'_p(y)dy\right), \tag{2}$$

where x_1 and y_1 are the attenuation path length of the primary beam and the secondary beam, respectively, as illustrated in the Fig. 1(B), and $\mu_p(x)$ and $\mu'_p(y)$ are the attenuation coefficients of the material along the paths of the primary beam and the secondary beam, correspondingly.

Considering the facts that the highest iodine concentration is 1.0% in our study and the attenuation coefficient of PMMA is similar to water, the calculation of the attenuation correction factor could be greatly simplified. Equation (2) can be simplified as:

$$\mathrm{C} = \exp\left(\mu_\mathrm{w} * \mathrm{x}_1 + \mu'_\mathrm{w} * \mathrm{y}_1\right), \tag{3}$$

where μ_w and μ'_w are the attenuation coefficients of water at the effective x-ray energy levels for the primary beam and the secondary beam, respectively. The secondary x-ray beam has an effective x-ray energy at the iodine fluorescence x-ray energy (28.6 keV). For the primary x-ray beam, only those x-ray photons with energies above 33.2 keV (the iodine K edge energy) in the excitation beam spectrum have the capability to excite the iodine atom to generate fluorescence x-rays.

Therefore, the effective energy ($\tilde{E}$) for the primary beam can be calculated by the following equation:

$$\tilde{E} = \frac{\int_{E=33.2keV}^{E=40keV} E \times w(E)\, dE}{\int_{E=33.2keV}^{E=40keV} w(E)\, dE}, \tag{4}$$

where $w(E)$ is the distribution of excitation x-ray beam at the energy E in the normalized excitation spectrum.

Finally, the fluorescence peak height (h) produced by the procedure described in the above section II.B.1) was multiplied by the attenuation correction factor (C) to obtain the XFMI signal. The final XFMI images were generated for the contrast phantom under two excitation spectra.

C. XFMI SYSTEM SIMULATION

Based on the theoretical model in Appendix, we can computationally simulate an XFMI system and calculate *the number of the generated fluorescence photons* (n) for a given XFMI system setup. We implemented the simulation program in Matlab to simulate the physical experiments using the same system geometrical protocol as described in Section II.A.

We used the calibration phantom (Fig. 2(A)) in our simulation and calculated the number of generated fluorescence photons (k_α peak) for the three excitation spectra (1.02 mm Cu filter, 5.20 mm Al filter, and 2.08 mm Al filter) at a fixed dose level of 200 mR. For the inserted iodine solution in the calibration phantom, we used a same series of iodine concentrations as we used in the experiment, which are1%, 0.5%, 0.25%, 0.167%, 0.125%, 0.1% and 0% (pure water) by weight (wt.)

To compare the simulation data with experimental data, we calculated the summation of net fluorescence signal for the k_α fluorescence peak energy range and the sum was considered the number of generated fluorescence photons corresponding to that obtained in the experiment. The comparison of the simulation data with the experimental data is plotted in Fig. 8. The Pearson Correlation Coefficient (PCC) is calculated between the experimental data and simulation data by the equation below. The result is also reported in the plots (Fig. 8).

$$PCC = \frac{\sum_i \left(n_i^e - \overline{n^e}\right) * \left(n_i^s - \overline{n^s}\right)}{\sqrt{\sum_i \left(n_i^e - \overline{n^e}\right)^2 * \sum_i \left(n_i^s - \overline{n^s}\right)^2}}), \tag{5}$$

where n_i^e is the experimentally measured number of the generated fluorescence photons (under concentration c_i), n_i^s is the corresponding simulated number of the generated fluorescence photons in the simulation, $\overline{n^e}$ is the mean of experimentally measured data under different iodine concentrations, and $\overline{n^s}$ is the mean of corresponding simulated data in the simulation.

III. RESULTS

A. EXCITATION BEAM SPECTRA

Fig. 4 displays the excitation spectra from the three filter options. It shows both the experimentally measured spectra and the simulated spectra from SpekCalc [38]. All the spectra are normalized for better visual comparison. A good match between the simulations and measurements can be observed in the figure, which also validates the dose calculation method adopted in this study.

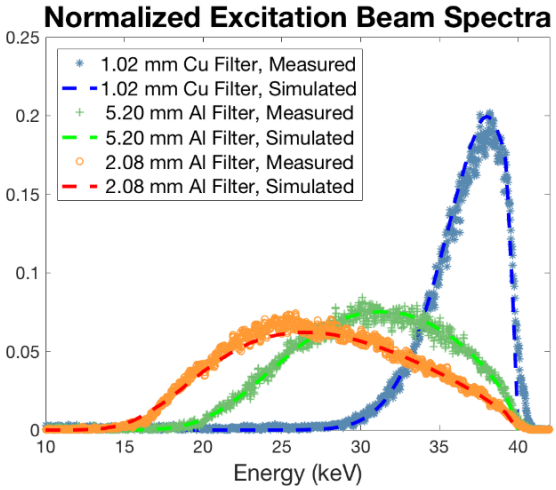

FIGURE 4. The normalized excitation spectra. The dots represent the experimentally measured data, and the dashed lines represent the simulated data from the SpekCalc.

B. LINEARITY BETWEEN NET FLUORESCENCE SIGNALS AND IODINE CONCENTRATIONS

The linearity between the net fluorescence signals and the corresponding iodine concentrations from the calibration phantom were investigated. Fig. 5 shows the three linear least- squares-fitted curves for the fluorescence peak heights from the three filter options (1.02 mm Copper,

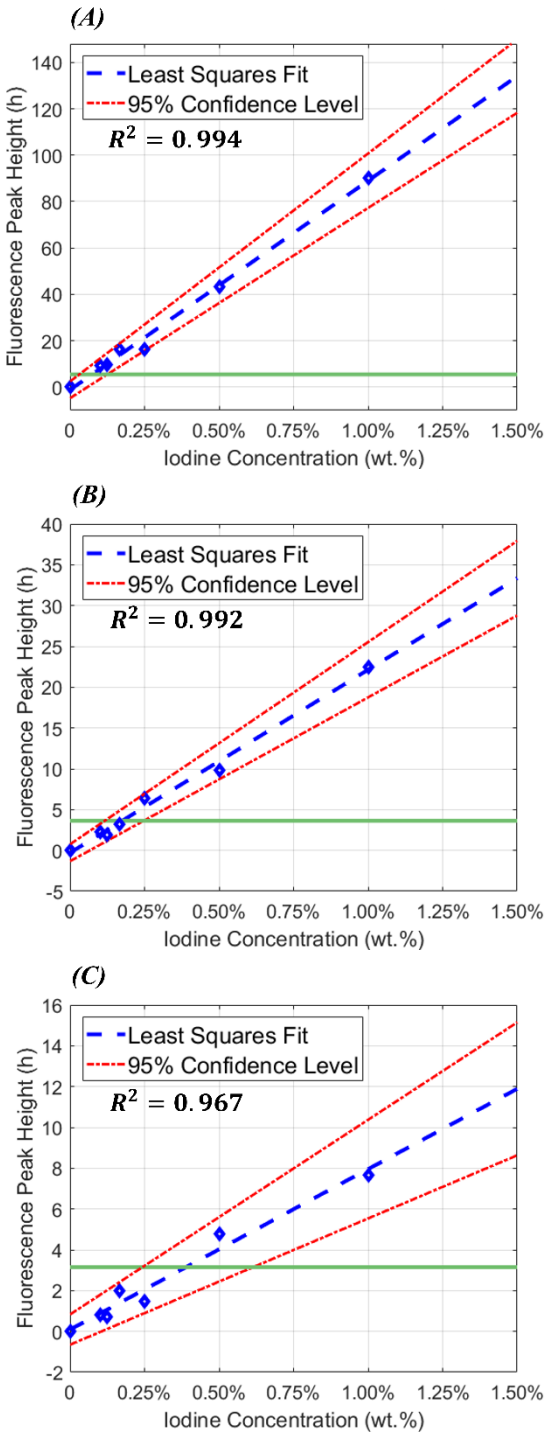

FIGURE 5. Linearity between the fluorescence peak heights and iodine concentrations under three excitation spectra. The blue dots are the experimentally obtained fluorescence peak heights at various concentrations, the dashed blue lines are the linear least squares fit to the fluorescence peak height data, the red dashed lines are the 95% confidence levels of the linear fits. The green solid lines are the $1.96\sigma_{bg}$ reference levels used to determine the MDCs. (A) 1.02 mm Cu Filter. (B) 5.20 mm Al Filter. (C) 2.08 mm Al Filter.

5.20 mm Aluminum, and 2.08 mm Aluminum). The linearity was characterized by the coefficients of determination (R^2), as displayed in the Fig. 5. The coefficients of determination are all larger than 0.95 for the experiments with three excitation spectra. This good linearity indicates that the net fluorescence signals from our XFMI system can be used for quantifying the iodine concentrations with high confidence.

C. MINIMUM DETECTABLE CONCENTRATION

Using the data from the calibration phantom, the MDCs were obtained for the three filter options as shown in Fig. 5. The best sensitivity (i.e. MDC with the smallest value) came from the excitation spectrum by the 1.02 mm Cu filter, with the MDC as low as 0.074%, as listed in Table 3. Compared to the MDC from the excitation spectrum by the 2.08 mm Al filter, the MDC from the excitation spectrum by the 5.20 mm Al filter was improved 2.22 times, and the MDC from the spectrum by the 1.02 mm Cu filer was improved 5.26 times. This demonstrates that the sensitivity of an XFMI system can be significantly increased by optimizing its excitation spectrum.

TABLE 3. Minimum detectable concentrations at three excitation spectra.

Different Excitation Spectra Group:	MDC (*wt.*)
1.02mm Cu filter:	$0.074\%\ ^{-0.043\%}_{+0.051\%}$
5.20mm Al filter:	$0.175\%\ ^{-0.059\%}_{+0.072\%}$
2.08mm Al filter:	$0.389\%\ ^{-0.146\%}_{+0.225\%}$

To find out the uncertainties of the MDCs, the 95% confidence levels of the linear fits to the fluorescence peak height data were plotted as the red dashed lines in Fig. 5. The intersection points of these 95% confidence level lines with the $\mathbf{1.96}\sigma_{bg}$ reference line can be used to find out the uncertainties of the derived MDCs, which are shown in Table 3.

D. XFMI IMAGE OF CONTRAST PHANTOM

The XFMI image of the contrast phantom is shown in Fig. 6. As can be seen from the figure, the positions of the three vials containing iodine solutions at three different concentrations are clearly visible, and the brightness of the three vials in the images correctly reflects the concentrations of the iodine solutions.

The XFMI signal at each vial location was plotted in Fig. 7. For each excitation spectra, linear least squares fit was applied to the XFMI signals at the three vial locations. As shown in Fig. 7, excellent linearity is observed ($\boldsymbol{R^2 > 0.97}$ for both fits), which indicates the high confidence of our XFMI technique in accurately mapping out the different iodine concentrations in single XFMI experiment. Furthermore, our results show that the excellent linearity ($\boldsymbol{R^2 > 0.97}$) between the XFMI signals and the iodine concentrations can be achieved for iodine concentration from 0.2% to 1.0%.

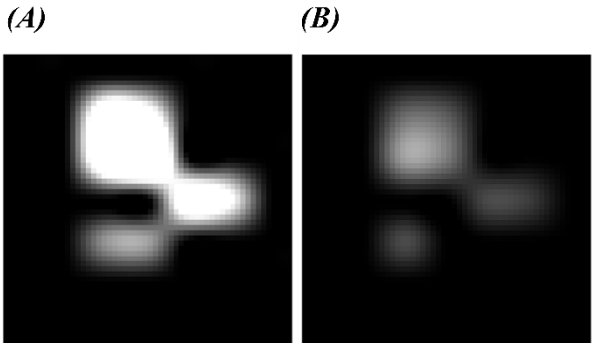

FIGURE 6. The XFMI images generated from the pixel-mapping method for the contrast phantom at two excitation spectra. The display window for the both images is [0, 40]. (A) XFMI Image 5.20 mm Al Filter. (B) XFMI Image 2.08 mm Al Filter.

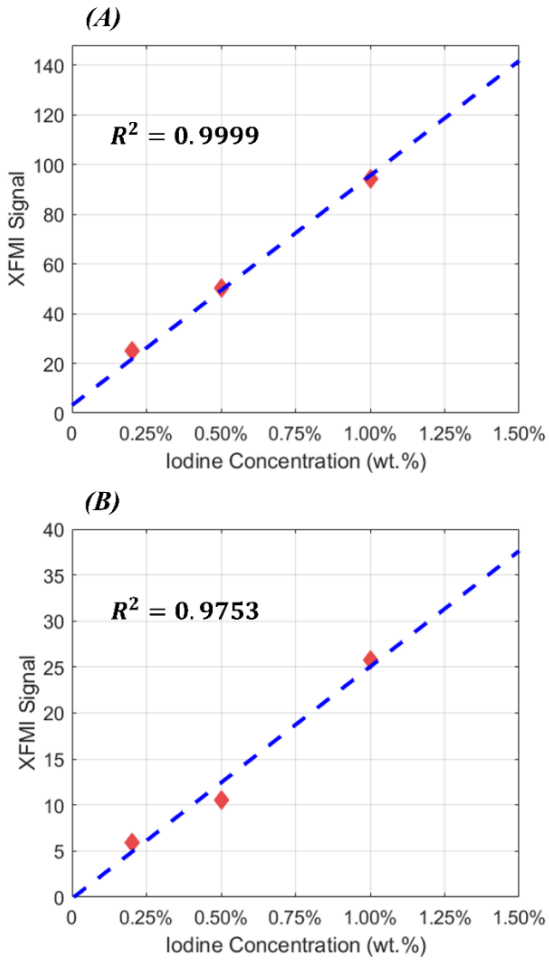

FIGURE 7. Linearity between the XFMI image signals and the iodine concentrations for the two XFMI experiments with (A) 5.20 mm Al filter, and (B) 2.08 mm Al filter.

E. SIMULATIONS VS. EXPERIMENTS

The comparison of simulation data with the experimental data is shown in Fig. 8. A good match between the experimental data with the simulation model can be visually observed. To obtain the quantitative analysis of the deviation between

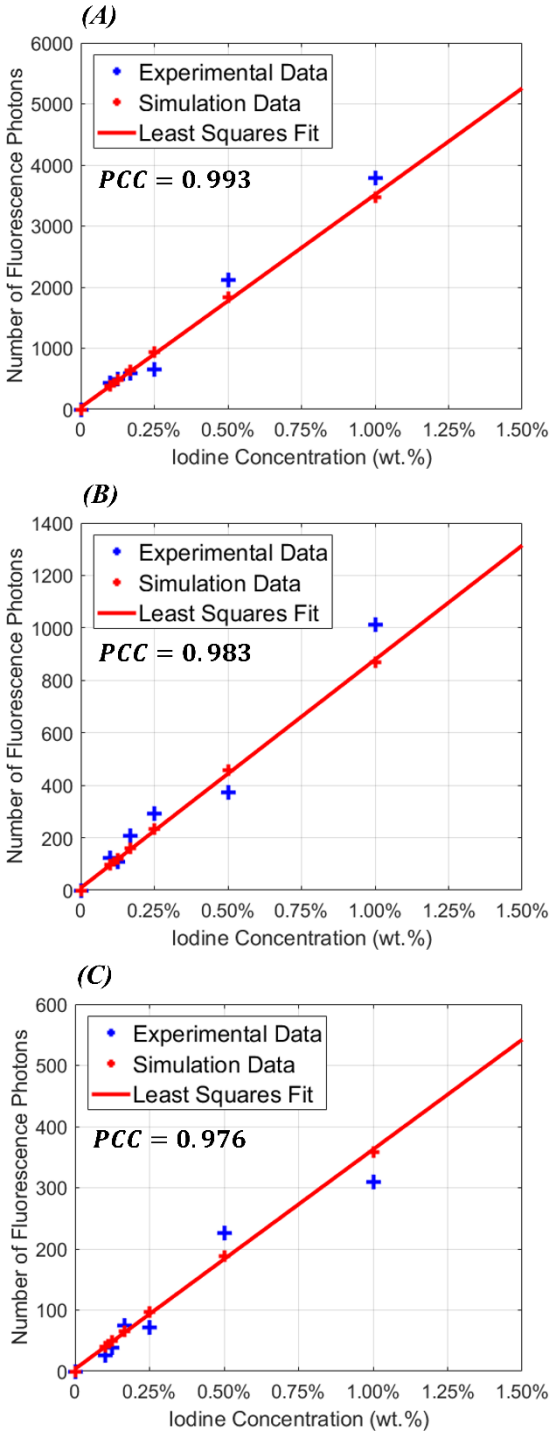

FIGURE 8. **The comparison of experimental data with simulation data. The blue dots are the number of generated fluorescence photons (k_α peak) at various concentrations in the experimental data, the red dots are the number of generated fluorescence photons (k_α peak) at various concentrations in the simulation data, and the red lines are the linear least squares fits to the simulation data. (A) 1.02 mm Cu Filter. (B) 5.20 mm Al Filter. (C) 2.08 mm Al Filter.**

the simulations and experiments, we report the PCC in plot. The simulation model is validated by the good agreement with the experimental data ($\boldsymbol{PCC > 0.976}$).

IV. DISCUSSION AND CONCLUSION

In this study, we experimentally investigated the impact of the excitation x-ray spectrum on the molecular sensitivity of XFMI in a pixel-mapping configuration. We investigated the effects of three distinctive excitation spectra, which were generated by changing the material and thickness of the x-ray source filter, on the XFMI imaging of a calibration phantom and a contrast phantom containing iodine solutions at low concentrations ($\leq 1\%$ wt.). We quantitatively determined the molecular sensitivity of the XFMI system using the minimum detectable concentration (MDC) of iodine. Our experimental results exhibit strong linearity between the fluorescence peak height and iodine concentration for the calibration phantom, as well as between the XFMI signal and iodine concentration for the contrast phantom. Furthermore, we developed an XFMI simulation model to simulate the XFMI system and validated the model with the experimental data. The good agreement ($\boldsymbol{PCC \geq 0.976}$) between the simulation and the experimental gives us high confidence in using the model to computationally search for an XFMI system that is optimized for a specific small-animal XFMI imaging task in future study.

We investigated the MDCs under different excitation spectra for a fixed surface entrance radiation dose level of 200 mR. The result showed that increasing the thickness of the x-ray source filter (from 2.08 mm All to 5.20 mm Al) led to 2.22 times improvement in the molecular sensitivity, and switching the filter to material with a higher atomic number (from 2.08 mm Al to 1.02 mm Cu) led to 5.26 times improvement in the molecular sensitivity. The results are in line with what one would expect. It is well known that x-ray fluorescence of an element can only be generated by those excitation x-rays whose energies are higher than the K-edge of the element. For the three excitation spectra used in our study, as shown in the Fig. 4, the spectrum generated by the 1.02 mm Cu filter contains the largest percentage of the effective x-rays that have the ability to generate x-ray fluorescence photons for iodine, and the spectrum generated by the 2.08 mm Al filter contains the smallest percentage of the effective x-rays. These results demonstrate the importance of optimizing the excitation beam spectrum for improving the molecular sensitivity in Bremsstrahlung x-ray source based XFMI.

This effect of the excitation spectrum on molecular sensitivity of XFMI was further validated via the XFMI of a mouse-sized contrast phantom that contains various iodine concentrations. The generated XFMI images are shown in Fig. 6. The XFMI image from the 5.20 mm Al filter clearly shows a better contrast between different iodine concentrations than the one from the 2.08 mm AL filter. Quantitatively, the contrast-to-noise ratio (CNR, defined as $\boldsymbol{CNR_{AB} = (Signal_A - Signal_B)/[(Noise_A + Noise_B)/2]}$) between the 1% iodine solution and the 0.5% solution is 18.73 in the XFMI image from the 5.20 mm Al filter and 11.09 in the XFMI image from the 2.08 mm Al filter. Fig. 7 shows the linearity between the XFMI image signals and the iodine concentrations. The slope of the linearly fitted line is referred as the

sensitivity of XFMI system in some publications [12], [39]. Based on the slope, the molecular sensitivity in our XFMI system was improved by a factor of 3.61 from optimizing the excitation spectrum by changing the x-ray source filter from 2.08 mm Al to 5.20 mm Al. This result is consistent with the MDC finding using the calibration phantom.

The excitation spectrum can be further optimized to get even better sensitivity. There are at least two possible approaches. One is to increase the x-ray tube voltage to get more effective x-rays that are capable of generating fluorescence signals. However, the efficiency of exciting x-ray fluorescence from the target element by an excitation photon will decrease as the energy of the excitation photon increases, which will lead to lower dose efficiency (defined as sensitivity normalize by the radiation dose). Another is to further optimize the excitation spectrum by more filtering, for instance using a thicker copper filter to obtain a larger percentage of effective x-rays. For this approach, heavier filtration to the excitation beam can lead to higher sensitivity but it also comes with a cost of degraded contrasts in the image if using such filtration configuration for K-edge imaging and a cost of reduced excitation x-ray beam intensity, which will lead to longer exposure time to obtain the same amount of fluorescence signals. For example, as shown in Table 2 in this study, the required mAs for the Copper filter is 2479 times higher than the required mAs for the 2.08 mm Aluminum filter. To compensate for the long exposure time, a higher x-ray source current can be adopted. For example, as shown in Table 2, we adopted different x-ray source currents for different excitation spectra. Therefore, for a given imaging task, a tradeoff between the excitation beam filtration, exposure time, and radiation dose has to be made. XFMI is inherently a molecular imaging modality. Similar to other existing molecular imaging modalities such as PET and SPECT, in the future XFMI can be combined with CT or MRI to receive both structure and physiological information.

The achievable detected concentration for XFMI of the gold nanoparticle reported by Cheong *et al.* [10] was 1.0% wt. at a dose of 200 R and a resolution of 0.1 mm. After that, the extensive researches have been done to increase the sensitivity of XFMI techniques using laboratory x-ray sources. For example, Jones *et al.* [13] reported the achievable gold nanoparticle concentration of 0.5% wt. at the dose of 20.4 R and a resolution of 3 mm in 2012 ; Ahmad *et al.* [17] detected the concentration of 0.25% wt. at the dose of 1.4 R and a resolution of 6.4 mm in 2015; and Manohar *et al.* [40] obtained the MDC as low as 0.24% wt. at the dose of 74.3 R and a resolution of 2.5 mm in 2016; Some relevant works have shown that applying a sheet-beam configuration was helpful for sensitivity improvement [41], [42], and optimizing detector angular configuration was able to achieve one order of magnitude increase in sensitivity [43], [44]. Here we report the best sensitivity of 0.074% (wt.) for 200 mR entrance dose at 3 mm spatial resolution for a laboratory x-ray source based XFMI system designed for small animal XFMI imaging. The improvement in sensitivity was achieved from excitation spectrum optimization via simple filtration. To obtain capability for *in vivo* clinical and pre-clinical XFMI, future research may incorporate the improvements made in excitation beam geometry, detector configuration, as well as excitation spectrum optimization.

XFMI of small animals, particularly mice and rats, will be valuable for many basic and preclinical studies. Improving the molecular sensitivity of XFMI system is the key to promote the application of XFMI technique. However, the molecular sensitivity of XFMI system is jointly affected by many factors, such as the detector configuration, the source configuration, the choice of contrast agent, and so on. As a result, comprehensive investigations on how different configurations affect the molecular sensitivity are significant in optimizing the XFMI system design. The primary focus of the study is to investigate the excitation beam optimization technique to improve molecular sensitivity of XFMI system. To the best of our knowledge, none of such systematic and experimental investigations on excitation spectrum optimization method to improve the XFMI molecular sensitivity has been conducted before. In addition, we developed an XFMI system simulation model based on the theoretical equations in Appendix, and validated the simulation model by the experimental data. The good agreement enables us to use the XFMI simulation model to do more complicated studies about how different factors have an influence on the molecular sensitivity of XFMI system and investigate various XFMI system configurations to further improve the molecular sensitivity, such as different x-ray source voltages, different anode materials, and so on. Using this model to investigate how to further optimize the XFMI system configuration to get higher molecular sensitivity will be our future research plan.

In conclusion, a systematic investigation of the effect of the x-ray excitation spectrum on the molecular sensitivity of the XFMI system has been reported in this paper. We designed and generated three different excitation spectra by altering the x-ray filter material and thickness, and applied them to the XFMI imaging of two iodine-containing phantoms. The results show that under optimized excitation beam, the molecular sensitivity of the XFMI system was demonstrated to be much improved. Furthermore, based on the experimental investigation, an XFMI simulation model was built and validated, which will find use for further improving the molecular sensitivity and guiding the XFMI system design in the future.

APPENDIX

In an XFMI system, an object is excited by an external primary x-ray beam, as shown in Fig. 1. The fluorescence signal could be generated only by those x-ray photons with energy higher than the K-edge energy (E_k) of the targeted element in the object. For iodine, $E_k = 33.2keV$. As a result, the number of fluorescence photons that are generated by an excitation x-ray beam at an interaction pixel is calculated as:

$$N_{fl} = \int_{E_k}^{E_{max}} \eta N_{(E)} \left(1 - exp(-\mu_{pe_{(E)}} * c * d)\right) dE, \qquad (6)$$

where $N_{(E)}$ is the number of x-ray photons at energy E for a given excitation spectrum, $\mu_{pe_{(E)}}$ is the photoelectric attenuation coefficient of the interacting material at energy E, c is the element molecular concentration, d is the attenuating length of the pixel, and η is the fluorescence yield of the target element. For iodine K shell, η is 0.884.

Considering that the fluorescence x-ray detector in the XFMI system is well collimated by a detector collimator, only a small portion of the generated fluorescence x-ray photons in a certain solid angle that is determined from the acquisition geometry can reach the fluorescence x-ray detector. As a result, the measured number of fluorescence x-ray photons at the detector is:

$$N_{fl}^{measure} = \frac{1}{4\pi} * \int N_{fl} d\Omega = \frac{1}{2} \int_{\theta_d - \frac{\Delta\theta}{2}}^{\theta_d + \frac{\Delta\theta}{2}} N_{fl} \sin(\theta)\, d\theta, \quad (7)$$

where θ_d is the angle between the excitation beam and the detector line of sight, which is 90 degree in our experimental setup, and $\Delta\theta$ is the angular range subtended by the x-ray detector sensor area after the detector collimation. The detailed geometrical illustration is shown in Fig. 1(B).

For the Rayleigh scatter, only those Rayleigh scatter x-ray photons with energy near the fluorescence peak energy (E_p) will interfere with the fluorescence signal measurement. Suppose the interfering Rayleigh scatter x-ray photon energy (E) ranges from $[E_p - \frac{\Delta E}{2}, E_p + \frac{\Delta E}{2}]$ (which happens to be the fluorescence peak energy range), the number of measured Rayleigh scatter x-ray photons can be calculated in a similar way:

$$\begin{aligned} N_{rs}^{measure} &= \frac{1}{4\pi} * \int N_{rs} d\Omega \\ &= \frac{1}{2} \int_{\theta_d - \frac{\Delta\theta}{2}}^{\theta_d + \frac{\Delta\theta}{2}} \int_{E_p - \frac{\Delta E}{2}}^{E_p + \frac{\Delta E}{2}} N_{(E)} \left(1 - exp(-\mu_{rs_{(E)}} * d)\right) dE \sin(\theta)\, d\theta, \end{aligned} \quad (8)$$

where $\mu_{rs_{(E)}}$ is the Rayleigh scatter attenuation coefficient of the interacting material at energy E.

For the Compton scatter, the energy of the x-ray photon will change by the Compton scatter interaction, as a result, the number of measured Compton scatter x-ray photons can be calculated as:

$$\begin{aligned} N_{cs}^{measure} &= \frac{1}{4\pi} * \int N_{cs} d\Omega \\ &= \frac{1}{2} \int_{\theta_d - \frac{\Delta\theta}{2}}^{\theta_d + \frac{\Delta\theta}{2}} \int_{E_1}^{E} {}_2N_{(E)} \left(1 - \exp\left(-\mu_{cs_{(E)}} * d\right)\right) dE \sin(\theta)\, d\theta, \end{aligned} \quad (9)$$

where $\mu_{cs_{(E)}}$ is the Compton scattering attenuation coefficient at the interacting x-ray energy (E). The integration energy range $[E_1, E_2]$ is the energy range for the excitation beam x-ray energy (E) before Compton scattering, which corresponds to the interfering Compton scatter x-ray photon energy (E') ranging from $[E_p - \frac{\Delta E}{2}, E_p + \frac{\Delta E}{2}]$. The relationship between the Compton scatter x-ray photon energy (E') and the excitation x-ray photon energy (E) is governed by the following equation:

$$E = E' \frac{511\ keV}{511\ keV - E'(1 - \cos\theta)}. \quad (10)$$

Therefore, the total number of measured x-ray photons at the fluorescence x-ray energy range $[E_p - \Delta E/2, E_p + \Delta E/2]$ in the XFMI setup illustrated in Fig. 1 is:

$$N^{measure} = N_{fl}^{measure} + N_{rs}^{measure} + N_{cs}^{measure}. \quad (11)$$

REFERENCES

[1] L. Ahlgren, K. Lidén, S. Mattsson, and S. Tejning, "X-ray fluorescence analysis of lead in human skeleton *in vivo*," *Scand. J. Work, Environ. Health*, vol. 2, no. 2, pp. 82–86, 1976.

[2] R. Cesareo and S. Mascarenhas, "A new tomographic device based on the detection of fluorescent X-rays," *Nucl. Instrum. Methods Phys. Res. A, Accel. Spectrom. Detect. Assoc. Equip.*, vol. 277, nos. 2–3, pp. 669–672, May 1989.

[3] J. P. Hogan, R. A. Gonsalves, and A. S. Krieger, "Fluorescent computer tomography: A model for correction of X-ray absorption," *IEEE Trans. Nucl. Sci.*, vol. 38, no. 6, pp. 1721–1727, Dec. 1991.

[4] T. Yuasa *et al.*, "Reconstruction method for fluorescent X-ray computed tomography by least-squares method using singular value decomposition," *IEEE Trans. Nucl. Sci.*, vol. 44, no. 1, pp. 54–62, Feb. 1997.

[5] P. J. La Rivière, "Approximate analytic reconstruction in X-ray fluorescence computed tomography," *Phys. Med. Biol.*, vol. 49, no. 11, p. 2391, 2004.

[6] A. Simionovici *et al.*, "High-resolution X-ray fluorescence microtomography of homogeneous samples," *IEEE Trans. Nucl. Sci.*, vol. 47, no. 6, pp. 2736–2740, Dec. 2000.

[7] J. F. Hainfeld, M. J. O'Connor, F. Dilmanian, D. N. Slatkin, D. J. Adams, and H. M. Smilowitz, "Micro-CT enables microlocalisation and quantification of Her2-targeted gold nanoparticles within tumour regions," *Brit. J. Radiol.*, vol. 84, no. 1002, pp. 526–533, 2011.

[8] N. Khlebtsov and L. Dykman, "Biodistribution and toxicity of engineered gold nanoparticles: A review of in vitro and *in vivo* studies," *Chem. Soc. Rev.*, vol. 40, no. 3, pp. 1647–1671, 2011.

[9] T. Takeda *et al.*, "X-ray fluorescent CT imaging of cerebral uptake of stable-iodine perfusion agent iodoamphetamine analog IMP in mice," *J. Synchrotron Radiat.*, vol. 16, no. 1, pp. 57–62, 2009.

[10] S.-K. Cheong, B. L. Jones, A. K. Siddiqi, F. Liu, N. Manohar, and S. H. Cho, "X-ray fluorescence computed tomography (XFCT) imaging of gold nanoparticle-loaded objects using 110 kVp X-rays," *Phys. Med. Biol.*, vol. 55, no. 3, p. 647, 2010.

[11] W. Cong, H. Shen, and G. Wang, "Spectrally resolving and scattering-compensated x-ray luminescence/fluorescence computed tomography," *J. Biomed. Opt.*, vol. 16, no. 6, pp. 066014-1–066014-7, 2011.

[12] K. Ricketts *et al.*, "A quantitative x-ray detection system for gold nanoparticle tumour biomarkers," *Phys. Med. Biol.*, vol. 57, no. 17, pp. 5543–5555, Sep. 2012.

[13] B. L. Jones, N. Manohar, F. Reynoso, A. Karellas, and S. H. Cho, "Experimental demonstration of benchtop X-ray fluorescence computed tomography (XFCT) of gold nanoparticle-loaded objects using lead- and tin-filtered polychromatic cone-beams," *Phys. Med. Biol.*, vol. 57, no. 23, pp. N457–N467, Dec. 2012.

[14] Y. Kuang, G. Pratx, M. Bazalova, B. Meng, J. Qian, and L. Xing, "First demonstration of multiplexed X-ray fluorescence computed tomography (XFCT) imaging," *IEEE Trans. Med. Imag.*, vol. 32, no. 2, pp. 262–267, Feb. 2013.

[15] M. Ahmad, M. Bazalova, L. Xiang, and L. Xing, "Order of magnitude sensitivity increase in X-ray fluorescence computed tomography (XFCT) imaging with an optimized spectro-spatial detector configuration: Theory and simulation," *IEEE Trans. Med. Imag.*, vol. 33, no. 5, pp. 1119–1128, May 2014.

[16] L. Ren, D. Wu, Y. Li, G. Wang, X. Wu, and H. Liu, "Three-dimensional X-ray fluorescence mapping of a gold nanoparticle-loaded phantom," *Med. Phys.*, vol. 41, no. 3, p. 031902, Mar. 2014.
[17] M. Ahmad, M. Bazalova-Carter, R. Fahrig, and L. Xing, "Optimized detector angular configuration increases the sensitivity of X-ray fluorescence computed tomography (XFCT)," *IEEE Trans. Med. Imag.*, vol. 34, no. 5, pp. 1140–1147, May 2015.
[18] C. Yoon, Y. Kim, and W. Lee, "3D non-destructive fluorescent X-ray computed tomography with a CdTe array," *IEEE Trans. Nuclear Sci.*, vol. 63, no. 3, pp. 1844–1853, Jun. 2016.
[19] D. Wu *et al.*, "Measurements of gold nanoparticle concentration with K-shell X-ray fluorescence spectrum," *Proc. SPIE* , vol. 10065, p. 100650M-1, 2017.
[20] S. Zhang, L. Li, and Z. Chen, "XFCT imaging system with pinhole collimation and attenuation correction," in *Proc. IEEE Nucl. Sci. Symp., Med. Imag. Conf. Room-Temp. Semiconductor Detect. Workshop (NSS/MIC/RTSD)*, Oct./Nov. 2016, pp. 1–4.
[21] T. Sasaya *et al.*, "Preliminary study on X-ray fluorescence computed tomography imaging of gold nanoparticles: Acceleration of data acquisition by multiple pinholes scheme," *Nucl. Instrum. Methods Phys. Res. A, Accel. Spectrom. Detect. Assoc. Equip.*, vol. 886, pp. 71–76, Apr. 2018.
[22] L. Li, S. Y. Zhang, R. Z. Li, and Z. Q. Chen, "Full-field fan-beam X-ray fluorescence computed tomography with a conventional X-ray tube and photon-counting detectors for fast nanoparticle bioimaging," *Opt. Eng.*, vol. 56, no. 4, p. 043106, Apr. 2017.
[23] M. Bazalova, M. Ahmad, G. Pratx, and L. Xing, "L-shell X-ray fluorescence computed tomography (XFCT) imaging of Cisplatin," *Phys. Med. Biol*, vol. 59, no. 1, pp. 219–232, 2014.
[24] M. Bazalova-Carter, M. Ahmad, L. Xing, and R. Fahrig, "Experimental validation of L-shell X-ray fluorescence computed tomography imaging: Phantom study," *J. Med. Imag.*, vol. 2, no. 4, p. 043501, 2015.
[25] N. Manohar, F. J. Reynoso, and S. H. Cho, "Experimental demonstration of direct *L*-shell X-ray fluorescence imaging of gold nanoparticles using a benchtop X-ray source," *Med. Phys.*, vol. 40, no. 8, p. 080702, 2013.
[26] G. Cao, J. Lu, and O. Zhou, "X-ray fluorescence molecular imaging with high sensitivity: Feasibility study in phantoms," *Proc. SPIE*, vol. 8313, pp. 83130S-1–83130S-6, Mar. 2012.
[27] T. Takeda *et al.*, "Iodine imaging in thyroid by fluorescent X-ray CT with 0.05 mm spatial resolution," *Nucl. Instrum. Methods Phys. Res. A, Accel. Spectrom. Detect. Assoc. Equip.*, vols. 467–468, pp. 1318–1321, Jul. 2001.
[28] D. Wu, Y. Li, M. D. Wong, and H. Liu, "A method of measuring gold nanoparticle concentrations by X-ray fluorescence for biomedical applications," *Med. Phys.*, vol. 40, no. 5, p. 051901, 2013.
[29] J. C. Larsson, W. Vågberg, C. Vogt, U. Lundström, D. H. Larsson, and H. M. Hertz, "High-spatial-resolution nanoparticle x-ray fluorescence tomography," *Proc. SPIE*, vol. 9783, p. 97831V, Mar. 2016.
[30] M. Shilo, T. Reuveni, M. Motiei, and R. Popovtzer, "Nanoparticles as computed tomography contrast agents: Current status and future perspectives," *Nanomedicine*, vol. 7, no. 2, pp. 257–269, 2012.
[31] K. Ricketts, C. Guazzoni, A. Castoldi, and G. Royle, "A bench-top K X-ray fluorescence system for quantitative measurement of gold nanoparticles for biological sample diagnostics," *Nucl. Instrum. Methods Phys. Res. A, Accel. Spectrom. Detect. Assoc. Equip.*, vol. 816, pp. 25–32, Apr. 2016.
[32] T. Takeda *et al.*, "Fluorescent X-ray computed tomography with synchrotron radiation using fan collimator," *Proc. SPIE, Med. Imag., Phys. Med. Imag.*, vol. 2708, pp. 685–695, 1996.
[33] W. Cong, H. Shen, G. Cao, H. Liu, and G. Wang, "X-ray fluorescence tomographic system design and image reconstruction," *J. X-Ray Sci. Technol.*, vol. 21, no. 1, pp. 1–8, 2013.
[34] G. C. Kagadis, G. Loudos, K. Katsanos, S. G. Langer, and G. C. Nikiforidis, "*In vivo* small animal imaging: Current status and future prospects," *Med. Phys.*, vol. 37, no. 12, pp. 6421–6442, 2010.
[35] C. T. Badea, M. Drangova, D. W. Holdsworth, and G. A. Johnson, "*In vivo* small-animal imaging using micro-CT and digital subtraction angiography," (in English), *Phys. Med. Biol.*, vol. 53, no. 19, pp. R319–R350, Oct. 2008.
[36] B. M. Tsui and D. L. Kraitchman, "Recent advances in small-animal cardiovascular imaging," (in English), *J. Nucl. Med.*, vol. 50, no. 5, pp. 667–670, May 2009.
[37] R. Weissleder, "Scaling down imaging: Molecular mapping of cancer in mice," (in English) *Nature Rev. Cancer*, vol. 2, pp. 8–11, Jan. 2002.
[38] G. Poludniowski, G. Landry, F. DeBlois, P. M. Evans, and F. Verhaegen, "SpekCalc: A program to calculate photon spectra from tungsten anode X-ray tubes," *Phys. Med. Biol.*, vol. 54, no. 19, p. N433, 2009.
[39] R. Van Grieken and A. Markowicz, *Handbook of X-Ray Spectrometry*. Boca Raton, FL, USA: CRC Press, 2001.
[40] N. Manohar, F. J. Reynoso, P. Diagaradjane, S. Krishnan, and S. H. Cho, "Quantitative imaging of gold nanoparticle distribution in a tumor-bearing mouse using benchtop X-ray fluorescence computed tomography," *Sci. Rep.*, vol. 6, Feb. 2016, Art. no. 22079.
[41] Q. Huo *et al.*, "Sheet-beam geometry for *in vivo* fluorescent X-ray computed tomography: Proof-of-concept experiment in molecular imaging," *Opt. Lett.*, vol. 33, no. 21, pp. 2494–2496, 2008.
[42] S. Jiang, P. He, L. Deng, M. Chen, and B. Wei, "Monte Carlo simulation for polychromatic X-ray fluorescence computed tomography with sheet-beam geometry," *Int. J. Biomed. Imag.*, vol. 2017, May 2017, Art. no. 7916260.
[43] H. Von Busch, G. Harding, G. Martens, J.-P. Schlomka, and B. Schweizer, "Investigation of externally activated X-ray fluorescence tomography for use in medical diagnostics," *Proc. SPIE*, vol. 5745, pp. 90–102, Apr. 2005.
[44] M. Sjölin and M. Danielsson, "Improved signal-to-noise ratio for non-perpendicular detection angles in X-ray fluorescence computed tomography (XFCT)," *Phys. Med. Biol.*, vol. 59, no. 21, p. 6507, 2014.

XU DONG received the bachelor's degree in physics from the University of Science and Technology of China. He is currently pursuing the Ph.D. degree with the Biomedical Engineering and Mechanics Department, Virginia Tech. He is currently a Research Assistant with Virginia Tech and is focused on developing novel computed tomography imaging technology for more than four years. His research areas cover medical image analysis and processing, deep learning and machine learning, and medical imaging techniques.

CHENG CHEN received the B.S. degree in hydraulic engineering from Tsinghua University, China, and the Ph.D. degree in civil and environmental engineering from Northwestern University. He is currently an Assistant Professor with the Department of Mining and Minerals Engineering, Virginia Tech. He is also a Faculty Research Fellow with the National Energy Technology Laboratory, Department of Energy, Virginia Tech. His research is focused primarily on the advanced numerical methods in porous media, rock characterization using high-resolution computed tomography and SEM imaging, and the applications to petroleum engineering, geologic carbon sequestration, and water resources.

GUOHUA CAO received the Ph.D. degree in physical chemistry from Brown University in 2005. After his post-doctoral trainings at Brown University and UNC-Chapel Hill from 2005 to 2007, he became a Research Assistant Professor with the Department of Physics and Astronomy, UNC-Chapel Hill, from 2008 to 2011. He is currently an Assistant Professor of biomedical engineering with the Department of Biomedical Engineering and Mechanics, Virginia Tech, Blacksburg, VA, USA. His research is directed at biomedical imaging, with a focus on developing novel imaging hardware and software for image acquisition and formation. He received a number of awards, including the NSF CAREER Award in 2014.